Soils and Rocks
www.soilsandrocks.com
An International Journal of Geotechnical and Geoenvironmental Engineering
ISSN 1980-9743
ISSN-e 2675-5475

Soil testing at different scales: from micro-experiments to field tests in earthworks

Enrique Romero[1,2#]

Article

Keywords
Microstructural tests
Element and field tests
Compacted soils
Earthworks
Engineered barriers

Abstract

Examples of upscaling phenomena with experimental techniques are presented and discussed within the framework of compacted soils for hydraulic and environmental earthworks and engineered barriers for the energy sector. A series of laboratory experiments at different scales are presented and interpreted to focus on the need for experimental upscaling in compacted soils since distinctive behavioural features can only be detected at specific length scales. Permeability results on fine-grained soils and artificially prepared sand/bentonite mixture at different scales will be discussed with microstructural tests regarding 'dry' or 'wet side' compaction, element and mock-up tests on compacted soils in the laboratory, and field tests on a compacted trial embankment and demonstration test to explore anisotropic and heterogeneous features. The presented examples will help to motivate new experimental research subjects and promote experimental protocols at different scales ranging from mm-scale (micro), cm-scale element tests, dm-scale mock-ups and m-scale (trial/demonstration tests) to help understand and approach some fundamental questions observed at the application scale of compacted soils.

1. Introduction

The first question that can arise is why we need to observe and approach phenomena at different scales of compacted soils used in earthworks. A partial answer to this question is that the phenomena we detect often depend on the scale of experimental observation. Distinct behavioural features are observed at specific length scales, where soil preparation in the laboratory and field compaction follow different procedures (usually with larger aggregate sizes in the field) and impact the variability of soil properties. However, despite this limitation, where experimental results may display some difficulty in upscaling, we must provide answers to real applications on compacted soils with the available experimental results.

Within this context, experimental techniques in the laboratory and the field should assist in observing and understanding processes at the different scales demanded in earthworks (pore/grain level, phenomenological scale, field scale). Therefore, they will allow expanding our capability to predict and upscale the response of compacted soils in real-life engineering applications with predictive modelling. To achieve this objective, it is necessary to pay attention to the following aspects

- To select adequate techniques and improve experimental protocols to the appropriate length scale (microstructural tests, element and boundary value problem laboratory tests);
- To use larger-scale setups (dm-scale mock-ups, 1-g and N-g physical model tests, field tests) to mimic and better predict the response of field applications with realistic material properties (compacted soils with heterogeneous and anisotropic properties affected by the scale) and boundary conditions.

The present contribution will consider two examples of earthworks to focus on the need for experimental upscaling in compacted soils. On the one hand, earthworks for zoned earth dams and embankments for a canal in areas with collapsible soils. On the other hand, a case of experimental upscaling of an engineered gas-permeable seal within earthworks for the energy sector, where compaction variability in dry density has been assessed, and permeability tests have been carried out at different scales. Therefore, different phenomena have been approached in these examples at varying observation scales (from pore/grain microstructural level, element tests, mock-ups, and field experiments to progressively upscale to the application).

Figure 1 presents a schematic of a zoned earth dam to show an example of earthworks that rely on laboratory and field experiments and monitoring data during construction, with selected scale-dependent aspects of compacted soil behaviour and size effects of coarse aggregates. Regarding the latter aspect, much effort has been placed into the behaviour of coarse-grained geomaterials at the single particle scale using a new range of apparatus and testing techniques (e.g.,

[#]Corresponding author. E-mail address: enrique.romero-morales@upc.edu
[1]Universitat Politècnica de Catalunya, Departament d'Enginyeria Civil i Ambiental, Barcelona, Spain.
[2]Centre Internacional de Mètodes Numèrics a l'Enginyeria, Grup de Geomecànica, Barcelona, Spain.

Submitted on August 5, 2024; Final Acceptance on August 9, 2024; Discussion open until November 30, 2024.
https://doi.org/10.28927/SR.2024.006024

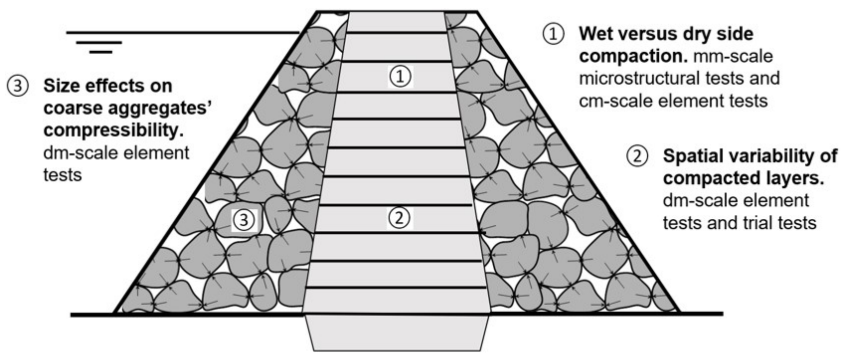

Figure 1. Selected aspects of compacted soil behaviour at different scales. Topics 1 and 2 are discussed in the paper.

Coop, 2024). Nevertheless, the large particle sizes in structures such as dams hinder laboratory testing. Predicting the field behaviour requires the development of discrete models that upscale (extrapolate) these effects from large-scale tests (e.g., Alonso et al., 2012; Alonso, 2014). Regarding earthworks for dams and embankments, the present contribution focuses on the compaction process when interpreted from a smaller-scale perspective ('wet' versus 'dry side' compaction) and the spatial variability in local dry density and anisotropy effects when viewed from a larger m-scale perspective (trial embankments).

2. Microstructural tests at mm-scale. 'Dry side' versus 'wet side' compaction

The state set on compaction (water content and dry density) substantially affects the hydro-mechanical behaviour of fine-grained soils used in zoned-earth dams and dikes. Besides the impact of the matric suction and maximum compaction stress of the compacted material (equivalent stress-based information to water content and dry density), the microstructure (connectivity of the larger pores and their sensitivity to loading, wetting and drying) also influences the behaviour (Romero et al., 2011; Casini et al., 2012; Romero, 2013; Alonso et al., 2013; Cordão Neto et al., 2017). An intuitive and straightforward way to differentiate this initial state is to refer to 'dry side' compaction with degrees of saturation S_r lower than the optimum reference (typically, the optimum water content and the maximum dry density correspond to S_r slightly above 85%) or to 'wet side' compaction with S_r higher than this reference. The 'dry side' compaction displays larger pore sizes due to fine-grain aggregation than the 'wet side', which impacts the properties dependent on the connectivity and the pore volume of these larger pores, such as water permeability, the water retention properties, the compressibility on loading (under unsaturated and saturated states) and the collapse on wetting. In addition to the initial state, the stress paths followed after the compaction (matric suction and net stress) influence the current pore size distribution (e.g., Yin & Vanapalli, 2022). Gonzalez-Blanco et al. (2023) proposed a stress-based equation using a single constitutive stress to discern the microstructural void ratio e_m of silty clay (voids inside the aggregates to the volume of solids) after different stress paths based on several controlled-suction oedometer tests followed by the determination of the pore size distribution by mercury intrusion porosimetry MIP on freeze-dried samples.

Figure 2 presents an alternative to this proposal, showing the macrostructural void ratio e_M (voids between aggregates to the volume of solids; $e_M = e\text{-}e_m$, where e is the void ratio) as a function of the S_r at compaction, which allows a more practical separation between the 'wet side' and 'dry side' domains outlined above and their microstructural consequences. It is essential to highlight the experimental difficulty involved in separating these intra- and inter-aggregate pore domains, in which more emphasis is placed on selecting the pore size based on the phenomena observed (e.g., intra-aggregate pore size domain with dominant water absorption mechanism and not affected by mechanical actions). Different alternatives of intra- and inter-aggregate separations are discussed in Yuan et al. (2020).

The soil corresponds to silty clay (58% < 75 μm with a liquid limit of 31%, a plasticity index of 12%, and a density of solids $\rho_s = 2.70$ Mg/m^3). As shown in the field emission scanning electron FESEM photomicrographs in the figure, the microstructure of a 'dry side' state develops aggregates with large and connected pores between these aggregations as opposed to a 'wet side' state. A pore size of 5 μm was used to separate the pore size domains using MIP on freeze-dried samples (macropore sizes > 5 μm were the only ones affected by loading at different S_r).

The e_M results are fitted to Equation 1 with two parameters $\alpha = 0.024$ and $\beta = 0.723$ (two different void ratios were considered in the plot, $e = 0.40$ and 0.80, to highlight its influence). Equation 1 is an updated expression that follows Romero et al. (2011) and Della Vecchia et al. (2013), which was already used by Romero et al. (2023) to interpret gas permeability.

$$\frac{e_m}{e} = \alpha + \beta S_r \le 1 \; ; \; \frac{e_M}{e} = 1 - \left(\alpha + \beta S_r\right) = 0.976 - 0.723 S_r \qquad (1)$$

To learn the utility of Equation 1, the results of cm-scale and controlled-gradient saturated permeability tests of the silty clay at different compaction states are presented in Figure 3a. Even if the compacted silty clay becomes saturated, it essentially retains the microstructural properties set during compaction. Consequently, the connected e_M of the 'dry side' compaction displays a permeability k one order of magnitude higher than the 'wet side' at the same $e = 0.571$ (corresponding to a dry density ρ_d = 1.70 Mg/m^3), as shown in the figure. Nevertheless, when compacting to the standard Proctor

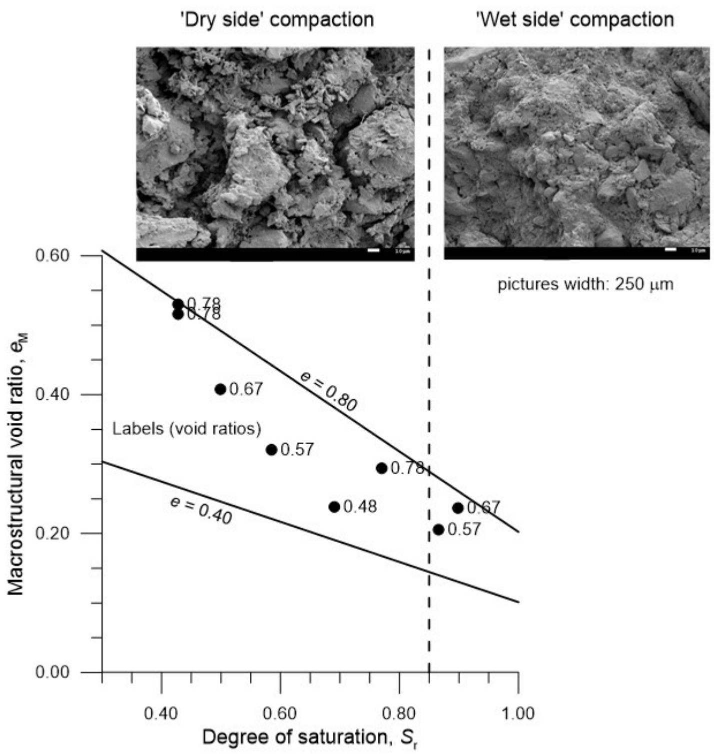

Figure 2. Macrostructural void ratio e_M as a function of S_r at compaction. Fitted curves for two different void ratios. Top: FESEM photomicrographs at two different hydraulic states ('dry side' and 'wet side' compactions) (the picture width is 250 μm) (data processed from Mora Ortiz, 2016).

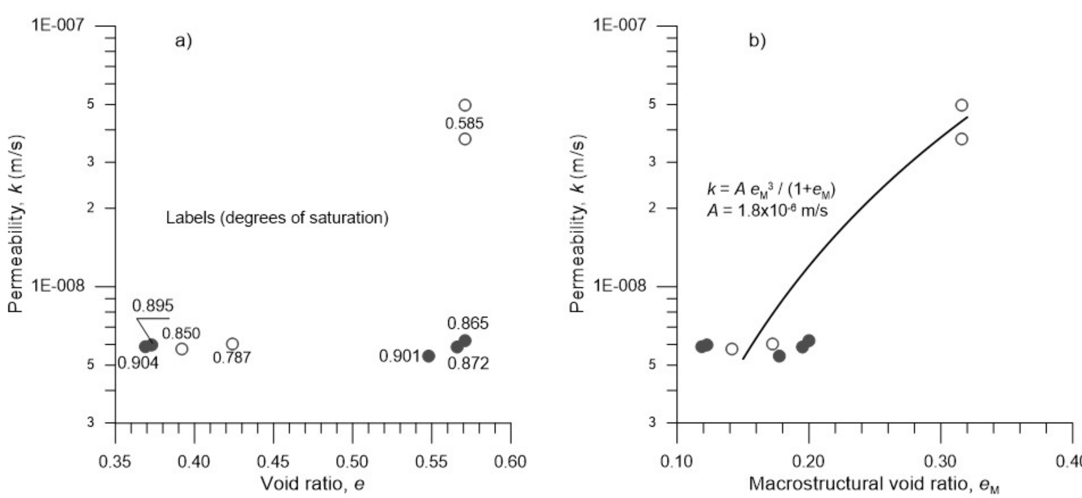

Figure 3. (a) Permeability k as a function of e (labels correspond to degrees of saturation at compaction, data processed from Mora Ortiz, 2016); (b) Permeability as a function of the macrostructural void ratio (Kozeny-Carman equation and as a function of e_M).

energy, the void ratio reduces to $e = 0.40$ ($\rho_d = 1.91$ Mg/m^3), and the difference in k between 'dry side' and 'wet side' compactions vanishes. Figure 3b plots k as a function of e_M calculated from Equation 1, in which high e values of the 'wet side' compaction are shifted to much lower e_M values. An expression based on the Kozeny-Carman equation and as a function of e_M is proposed in Figure 3b. It is essential to highlight that these results and their interpretation are based on cm-scale permeability tests and mm-scale mercury intrusion porosimetry results on freeze-dried samples after compaction (Romero & Simms, 2008).

3. Microstructural tests at mm-scale. Drying after compaction

Another phenomenon with practical implications and interpreted by microstructural tests is the increase in collapse after a silty clay is compacted and undergoes drying. The natural material corresponds to lightly cemented low-density silty clay (86% < 75 μm with a liquid limit of 33%, plasticity index of 16% and $\rho_s = 2.70$ Mg/m^3), prone to collapse upon wetting. One of the procedures envisaged to avoid damage to the canal embankments placed on these collapsible soils that may reach 10 m thickness was to replace the natural low-density soil with the same material but compacted to a higher dry density (Alonso et al., 2005). The geographical area of the canal is relatively arid. It has an annual mean rainfall in the range of 400-500 mm, which explains why it is essential to consider some desiccation of the compacted material. However, water losses from the canal may change this scenario dramatically after construction and increase the compacted material's degree of saturation, as Alonso et al. (2005) explained.

Figure 4 presents the initial state 'A' of the natural material in the compaction plane (corresponding to e = 1.06 and $S_r = 0.33$), which was compacted at standard Proctor energy and optimum water content (state 'B' in the figure at $e = 0.44$ and $S_r = 0.91$). The modified Proctor state at optimum water content is also indicated in the figure (e = 0.33 and $S_r = 0.92$). State 'C' ($e = 0.41$ and $S_r = 0.37$) is reached after drying the soil to a total suction $s = 26$ MPa (i.e., relative humidity around $RH \approx 82\%$) measured with a WP4C dew point psychrometer from METER Group. An environmental scanning electron (ESEM) photomicrograph at the corresponding water content is shown in the figure at state 'C', where fine-grain aggregates and macropores between them are observed despite the high dry density achieved on compaction and subsequent shrinkage.

Figure 5 presents results under oedometer conditions of collapse on wetting at different vertical stresses of the various states considered (natural, compacted and dried after compaction). The maximum collapse (vertical strain under oedometer conditions) of the low-density natural material reached 10.6% at 200 kPa. The lightly cemented low-density silty clay with gypsum and carbonate types of cement is relatively rigid up to vertical stress of 200 kPa, and the macropores are preserved. Nevertheless, cementation is lost on wetting, and a significant collapse develops. At a vertical stress of 400 kPa, some of the cementation is

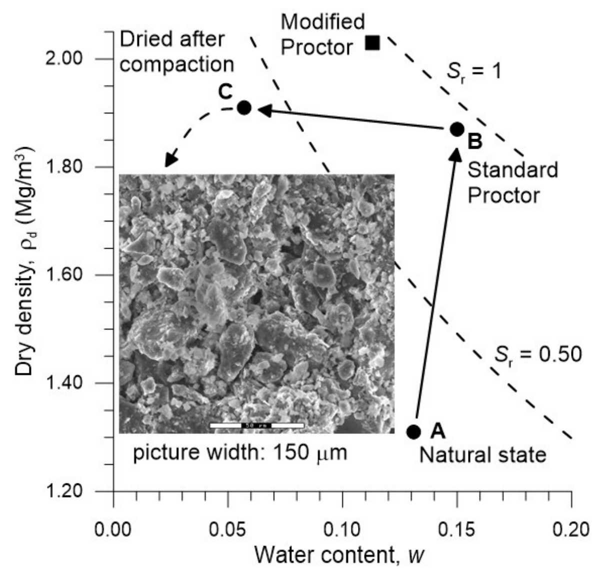

Figure 4. Natural 'A', compacted 'B' and dried after compaction 'C' states of a silty clay plotted in the Proctor plane. ESEM photomicrograph at state 'C' (the picture width is 150 μm).

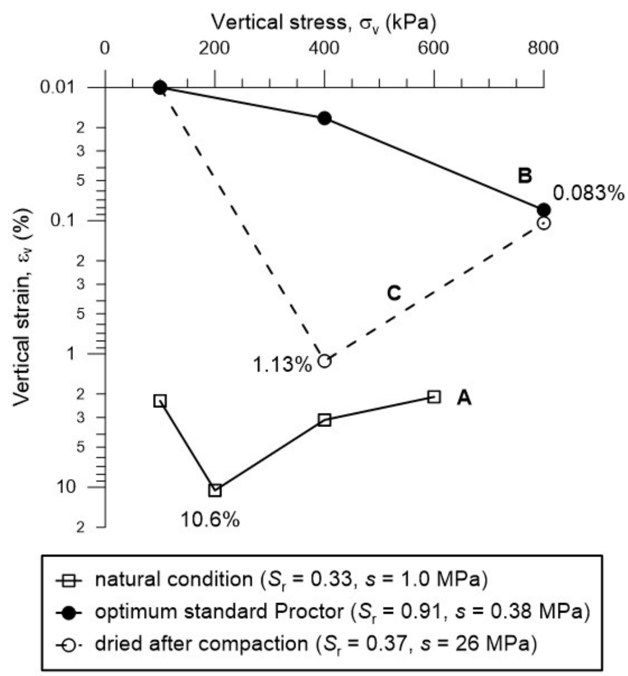

Figure 5. Collapse undergone on wetting under oedometer conditions: natural 'A', compacted 'B' and dried after compaction 'C' states of a silty clay. Legend: initial states before loading.

already lost by loading, and the material does not develop as much collapse when wetted. However, this framework changes drastically when compacting the material (the standard Proctor test is equivalent to a vertical stress of about 0.8 MPa, and the matric suction reaches $s = 0.38$ MPa measured with a high-range tensiometer) as the cementation is destroyed and the macropores are drastically reduced. The Barcelona Basic Model BBM (Alonso et al., 1990) predicts the development of the maximum collapse (plastic compression) at 800 kPa vertical stress when the loading-collapse LC curve is fully activated during wetting (maximum collapse 0.083%). Suppose the compacted material can dry by arid climate conditions (state 'C') above the maximum matric suction ever undergone. In that case, some irreversible shrinkage will occur by activating the suction-increase SI yield locus. Therefore, some strain hardening is expected to be generated during this irreversible shrinkage (BBM, Alonso et al., 1990). Nevertheless, the material is more prone to collapse despite the overall hardening, as shown in Figure 5, where a maximum collapse of 1.13% is reached at 400 kPa. Afterwards, increasing the vertical stress to 800 kPa reduces the collapse deformation since the material decreases the macroporosity and reaches higher degrees of saturation upon loading.

The explanation behind the enhancement of collapse on shrinkage is associated with the microstructural changes undergone during drying (enlargement of macroporosity between aggregates and fissuring). Figure 6 shows the evolution of the void ratio during suction increase from the compacted state 'B' to the dried state after compaction 'C'. The change in e is relatively small despite the significant suction change due to the silt shielding skeleton limiting this global shrinkage. As the figure shows, the microstructural void ratio is also affected and is associated with the aggregates' more significant and less constrained shrinkage. This shrinkage can be estimated using Equation 1 by calculating the variation of e_m/e with S_r and considering $e = 0.44$ (the initial value of the compacted state). Results of the microstructural void ratio determined by MIP on freeze-dried samples and reported by Romero (2013) for silty clays at $e \leq 0.44$ are also plotted, which also agree with the adopted trend. As shown in the figure, the difference between e and e_m (i.e., the macrostructural void ratio e_M) increases on drying (from $e_M = 0.14$ at 'B' to $e_M = 0.29$ at 'C') due to the opening of the macroporosity and fissuring. This increase in the macroporosity, also observed in the ESEM photomicrograph in Figure 4 between aggregates, can explain the enhancement of the collapsibility after a drying event. Alonso et al. (1999) also considered the macroscopic void ratio enlargement on drying on some materials when extending BBM to active soils during cyclic wetting and drying cycles. Although the change in e_M predicts a significant collapse if all the generated macroporosity vanishes on saturation, it does provide evidence of a phenomenon that can only be explained at this microstructural mm-scale.

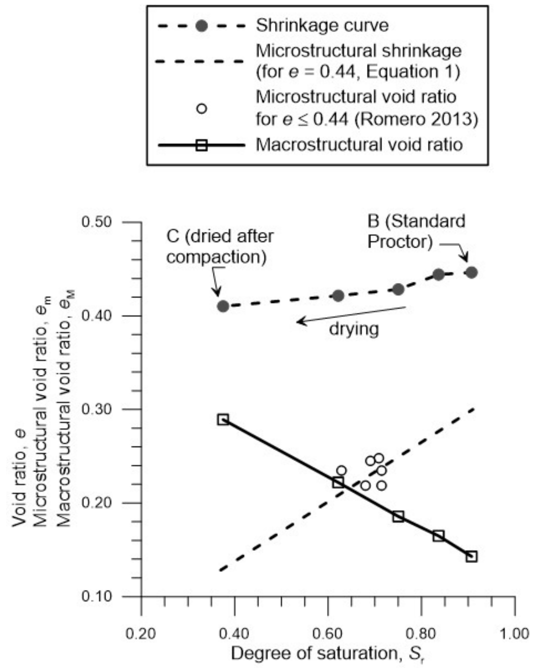

Figure 6. Evolution of e, e_m and e_M on drying after compaction. The evolution of the e_m is estimated from Equation 1 and results reported by Romero (2013).

4. Laboratory versus field dynamic compaction. Compaction-induced spatial variability in dry density

It is widely accepted that difficulties arise when characterising the hydro-mechanical behaviour of the compacted materials with laboratory tests and comparing the modelled response against field tests and monitoring data. Besides the uncertainty of S_r (or the matric suction), some uncertainties depend on the observation scale. It is generally found that permeability values measured in the laboratory are lower (sometimes by two orders of magnitude) than field measurements and that stiffness on loading is higher in the laboratory than in the field data. Pinyol & Alonso (2019) observed an example of the latter aspect when simulating the 90 m high Albagés zoned earth dam (Lleida, Spain). The authors modelled the dam construction using a numerical code dealing with unsaturated–saturated soils and the coupled hydro-mechanical phenomena (generation and dissipation of pore pressures and the corresponding mechanical response). The cm-scale element tests allowed a rigorous calibration of the model stiffness, which depends on the stress state (matric suction and net stress) and the preconsolidation stress of the compacted material, which also depends on matric suction. However, the authors consistently observed larger vertical field settlements than class A predictions using laboratory information along a vertical central section throughout the core. An updated model was also presented, considering compaction data and field tests performed during construction (information came from plate loading/unloading tests on the embankments), which allowed for better modelling of the vertical displacement response. Despite the lower degree of saturation and the consequences of matric suction on stiffness, the dm-scale plate loading tests allowed averaging of properties over a larger volume where local inhomogeneities on field compaction are captured. Lower mean dry density was achieved under field conditions due to the consequences of compacting on the 'wet side'.

To better understand this dynamic compaction-induced variability and its consequences on dry density and permeability anisotropy, Figure 7 presents the results of two compaction techniques in terms of *e* using tests at the dm scale (100-mm inner diameter PVC cylinder and 300 mm in height treated to minimise inner wall friction that microfocus X-ray CT verified). Sakaki et al. (2023) reported these tests on a sand/bentonite S/B mixture (80% by mass of SiO_2 sand and 20% Wyoming-type bentonite) at a water content of 11.0%. The Wyoming-type of bentonite presents 85% by mass of montmorillonite, and the mixture displays ρ_s = 2.66 Mg/m^3. The authors used static compaction (controlled displacement conditions up to 4.9 MPa and target *e* = 0.56) and dynamic compaction considering controlled energy per volume via dropping a mass with a smaller diameter (24 mm) at a certain height (a single layer was used mimicking field emplacement and the total compaction energy per unit volume corresponded to 1800 kJ/m^3 and target *e* = 0.59). The compaction-induced variability was characterised by slicing. As observed in the figure, the dry density along the static procedure was relatively homogeneous (*e* varying between 0.523 and 0.606), which was not the case with the dynamic compaction that led to a minimum void ratio of *e* = 0.395 at the top compaction surface and *e* = 0.755 close to the bottom boundary. A slight decrease in the void ratio is detected at the rigid bottom boundary with no displacement allowed (this bottom boundary condition is somehow different to that expected under field conditions).

A similar pattern using dynamic field compaction leading to higher dry density at the compaction surface was also observed in the large-scale 'GAs permeable Seal Test' GAST launched at Nagra's Grimsel Test Site GTS (Nagra stands for 'National Cooperative for the Disposal of Radioactive Waste', Switzerland) (Nagra, 2024; Rüedi et al., 2012; Sakaki et al., 2023). This test placed in a tunnel in granitic rock demonstrated the effective functioning of an engineered gas-permeable seal concept during gas transport after long-term saturation for a deep geological repository for low and intermediate radioactive waste mainly produced by the energy/medicine/industry sectors (Romero et al., 2023). The cylindrical S/B seal with a diameter of 3.0 m and 8.0 m long consists of 28 horizontal layers (100 mm in height) of dynamically compacted S/B as above (water content of 11.0%) using a vibratory plate (central part) and rammer compaction (near-wall areas). The field compaction was controlled by two procedures: a) controlled mass in 0.10 m layer with known total volume, and b) by sampling method from the top 20 mm of each layer (ring cutter at compaction surface with diameter 50 mm and height 20 mm). Figure 8 shows the void ratio variation with seal height for the different layers

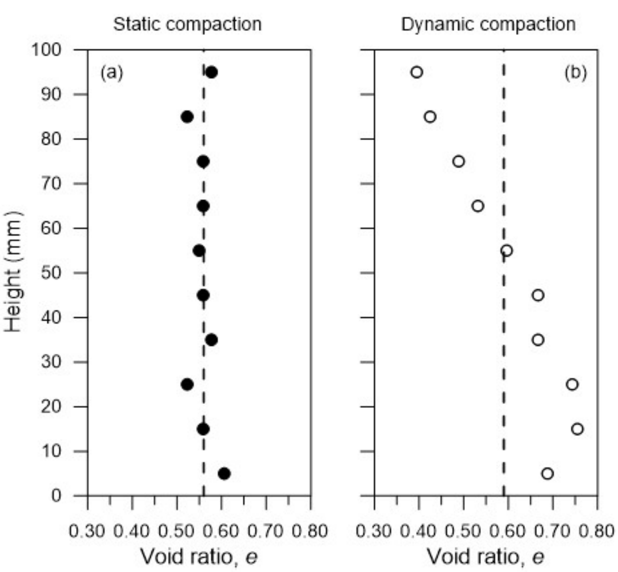

Figure 7. Evolution of *e* throughout the final compaction height (around 100 mm). (a) Static compaction; (b) dynamic compaction (data from Sakaki et al., 2023).

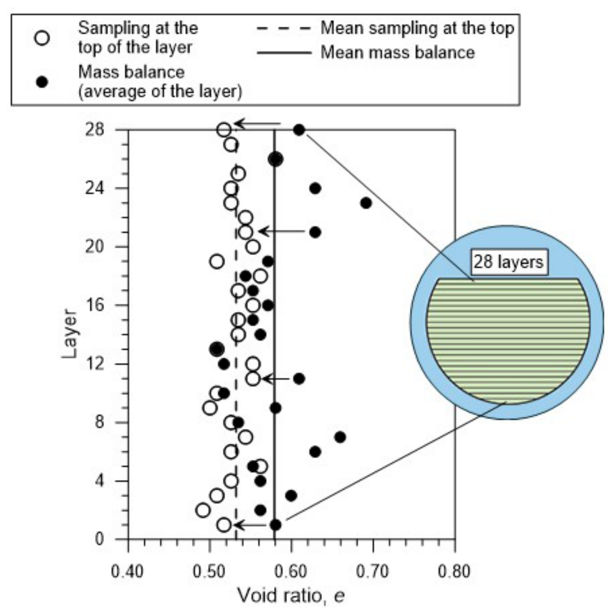

Figure 8. Evolution with height of *e* in each layer by mass balance method (layer average) and sampling (top 20 mm of the layer). The mean sampling results at the top of each layer displayed a lower *e* (data from Sakaki et al., 2023).

obtained by the mass balance method (average throughout the 8 m long layer) and ring cutter sample results (mean void ratio representative of the top compaction surface of each 8-m long layer). As observed, the samples retrieved from the top 20 mm usually reached lower void ratios (refer to the direction of the arrows in the figure) with a mean void ratio throughout the 2.8 m height of e = 0.532 (associated with ρ_d = 1.74 Mg/m^3). The mean void ratio of the mass balance method throughout the 2.8 m height (representative of the layer average) is e = 0.579, which is associated with ρ_d = 1.68 Mg/m^3 (layer average values display more considerable variability between e = 0.509 and 0.691, corresponding to ρ_d = 1.57 and 1.76 Mg/m^3). The mean bottom dry density throughout the height is expected to be ρ_d = 1.63 Mg/m^3. Therefore, there is a vertical zigzag variation of dry density in the field with lower void ratios at the top of each layer consistent with the single-layer compaction at the laboratory scale, which strongly impacts the permeability, as discussed in section 5.

Referring to the case of the Albagés zoned earth dam (Pinyol & Alonso, 2019), a distinctive aspect of the project was the execution of a trial embankment during the design phase. This innovative approach addressed the inherent shortcomings of laboratory small-scale tests of compacted samples in accurately reflecting geotechnical properties at full scale (performing vertical and horizontal field permeability tests and stiffness properties by plate loading/unloading tests). Moreover, the trial embankment facilitated an in-depth exploration of the compaction technique at a larger scale and different heights of the compaction layer. The 6-layer embankment was constructed with a lift thickness of 0.25 to 0.35 m (the first two layers 1 and 2 at 0.25 m, layers 3 and 4 at 0.30 m and final layers 5 and 6 at 0.35 m). Besides the variation in thickness, each lift was compacted with different wetting protocols and combinations of equipment, including sheepsfoot rollers with two masses and vibratory compactors at two frequencies (the number of passes, passing over the same point twice in each pass, was between 4 and 10 for each lift).

Figure 9 summarises laboratory data in the Proctor plane (standard energy 600 kJ/m^3, double standard energy and modified energy 2700 kJ/m^3) and field information. The dry densities and water contents at two different depths of each field compacted layer (at 0.05 m and 0.20 m from the top) are shown in the figure. The arrows indicate the deep-shallow evolution of the different lifts' dry density and water content. In general, the compaction zone close to the surface presents higher dry densities than the deeper ones (except for layer 6 and since in layer 2 no significant variation was detected), tending to the zigzag pattern in dry density described above. As observed, S_r varied between 0.6 and 0.8 (except for layer 3), which tends to the dry side due to the semiarid conditions of the site with an average rainfall of 400 mm/year (Lleida, Spain). This drier condition

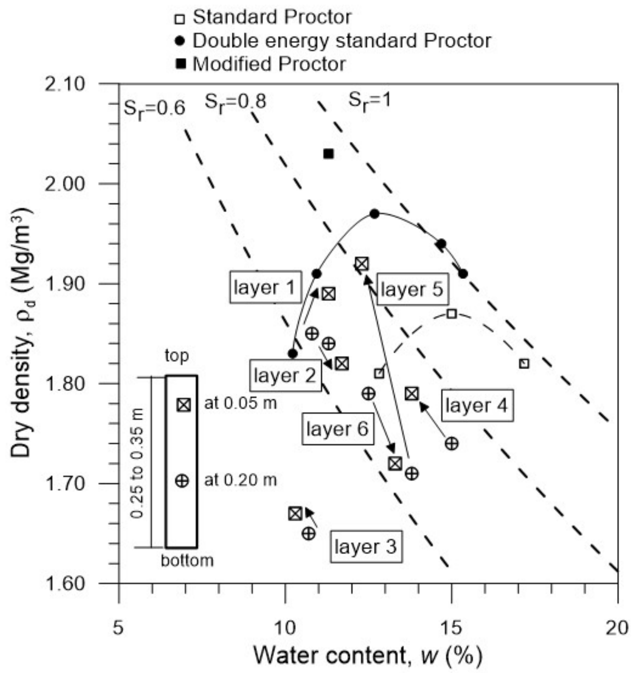

Figure 9. Compaction laboratory data (standard energy, double standard energy and modified energy) and field information of a trial embankment with six lifts of around 0.25-0.35 m thick. The arrows indicate the deep-shallow evolution of the different lifts' dry density and water content.

presents higher stiffness and hinders the achievement of high dry densities, particularly on layer 3.

5. Laboratory versus field compaction. Effects on permeability

The pattern mentioned above of zigzag variation of dry density in field compaction with a tendency towards lower e at the compaction surface has essential implications for permeability. The horizontal permeability (weighted arithmetic mean) reflects the higher permeability of the horizontal lifts at higher e (bottom of the layer). The high-density compaction surfaces condition the lower vertical permeability (weighted harmonic mean). This generates an anisotropy in the hydraulic response, whose interpretation depends on the experimental observation scale. The induced anisotropy, associated with a continuum approach, arises due to preferential vertical straining during 1-D static compaction (the usual way to reach a target dry density). This preparation technique affects the mechanical response (transversally isotropic fabric) and the permeability. Layering at a larger field compaction scale involves interfaces between lifts and low-density zones in the lift, which induces a layered structure with preferential pathways for water flow.

The first example to discuss involves the case of the Albagés zoned earth dam project (Pinyol & Alonso, 2019), where permeability at the laboratory scale (natural and compacted samples from the field test) and field scale (trial embankment) are presented. Figure 10 summarises laboratory results at the cm-scale using controlled gradient tests under isotropic conditions (samples 50 mm in diameter and 100 mm high). Different test procedures were selected. First, field-compacted samples were retrieved from the trial embankment and then trimmed to the dimensions of a triaxial specimen at different isotropic stresses (150 and 450 kPa) and two orientations (these field-compacted samples are indicated as FCH and FCV for the horizontally and vertically oriented samples, respectively). Second, natural samples from the lightly cemented low-density silty clay with gypsum and carbonate types of cement were retrieved, trimmed to the triaxial dimensions, loaded at different isotropic stresses and finally saturated before determining the vertical permeability (NL and NH, at low and high confining stresses undergoing different collapse strains on saturation). The figure also includes field test results on the trial embankment using permeameters for vertical permeability (TEV) and Lefranc-type tests for horizontal permeability (TEH) once the embankment was completed. The figure also labels the degree of saturation before permeability determination. A second permeability determination was carried out in layers 2, 5 and 6 in the vertical permeability tests.

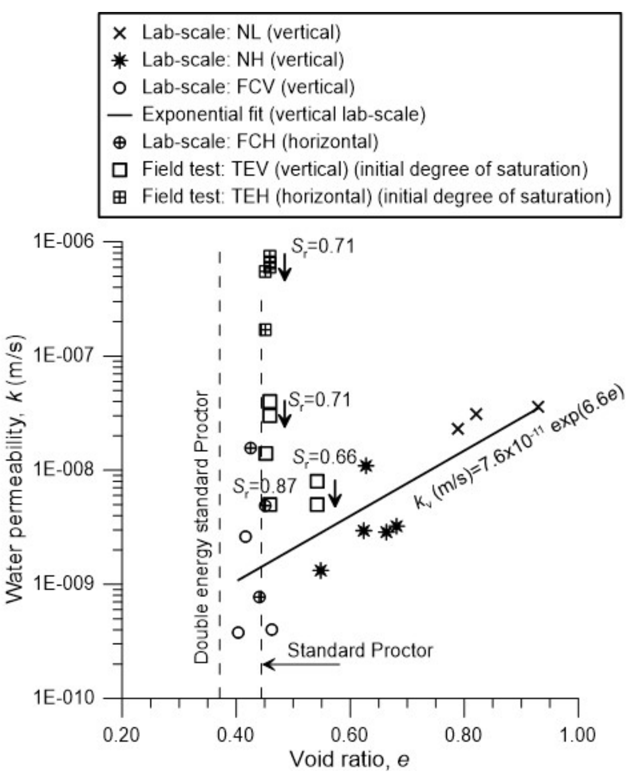

Figure 10. Permeability k at laboratory and field scales on field compacted samples at different orientations. Permeability of natural samples at different e.

The field tests capture the anisotropy induced by field compaction. The horizontal permeability (mean $k_h = 5.4\times10^{-7}$ m/s) was higher than the vertical permeability ($k_v = 1.7\times10^{-8}$ m/s) with an anisotropy ratio of around $k_h / k_v = 32$ due to preferential paths through potential interfaces and low-density zones in compaction layers (the zigzag pattern above). The permeability deduced from the field test is difficult to interpret since the compacted soil is not initially saturated. This implies that the actual infiltration gradients are different due to the incorporation of the matric suction potential (the vertical permeability slightly reduces on the second repetition of the test, as indicated by the arrows in the figure). On the other hand, the lack of saturation also modifies the permeability. The cm-scale tests in the laboratory for the fully saturated field compacted material indicated lower vertical permeability (mean $k_v = 1.1\times10^{-9}$ m/s; i.e., around one order of magnitude compared to field data) and lower horizontal permeability (mean $k_h = 7.1\times10^{-9}$ m/s) with a smaller anisotropy ratio $k_h / k_v = 7$. An expression for vertical permeability as a function of void ratio is included for lab-scale data. These results show the need to consider testing at different scales to better estimate the real application's conditions. While the tests at different scales provided reasonable control of e (references for the standard Proctor and double energy of standard Proctor are indicated in the figure), it was not the case for S_r. Differences are associated with the stress paths followed in the laboratory and field compactions, usually with distinct aggregate sizes and different procedures to transfer the compaction energy, which induce variability in dry density that depends on the scale and affects local pathways for water flow.

To better assess permeability on compacted soil at different scales with a well-controlled initial state (e and S_r), the results presented by Romero et al. (2023) associated with the field test 'GAs permeable Seal Test' GAST described in section 4 will be discussed. The study delves into process upscaling through different experimental techniques considering cm-scale element tests, innovative dm-scale mock-ups and m-scale demonstration tests (Nagra, 2024, GTS, Switzerland). The material is an artificially prepared sand/bentonite S/B mixture (80% SiO_2 sand and 20% Wyoming-type bentonite by mass described in section 4). Figure 11a shows the dm-scale mock-up (500 mm long and 300 mm in diameter). The mock-ups' semi-cylindrical shape facilitated the emplacement of dynamically compacted S/B layers with layer-parallel flow conditions (the hydraulic gradient was controlled at the lateral filter-to-filter boundaries), mimicking the field demonstrators' geometry. A mobile lid was designed to apply the necessary vertical stress and upper displacement to simulate constant volume conditions and mitigate any by-pass flow through steel/soil interfaces (a 10-mm thick granular bentonite layer was also placed at this interface). The S/B was emplaced in three layers of 75 mm thickness (with three controlled sub-layers) by dynamic compaction at standard Proctor energy of 600 kJ/m^3 (Figure 11b). The initial conditions of

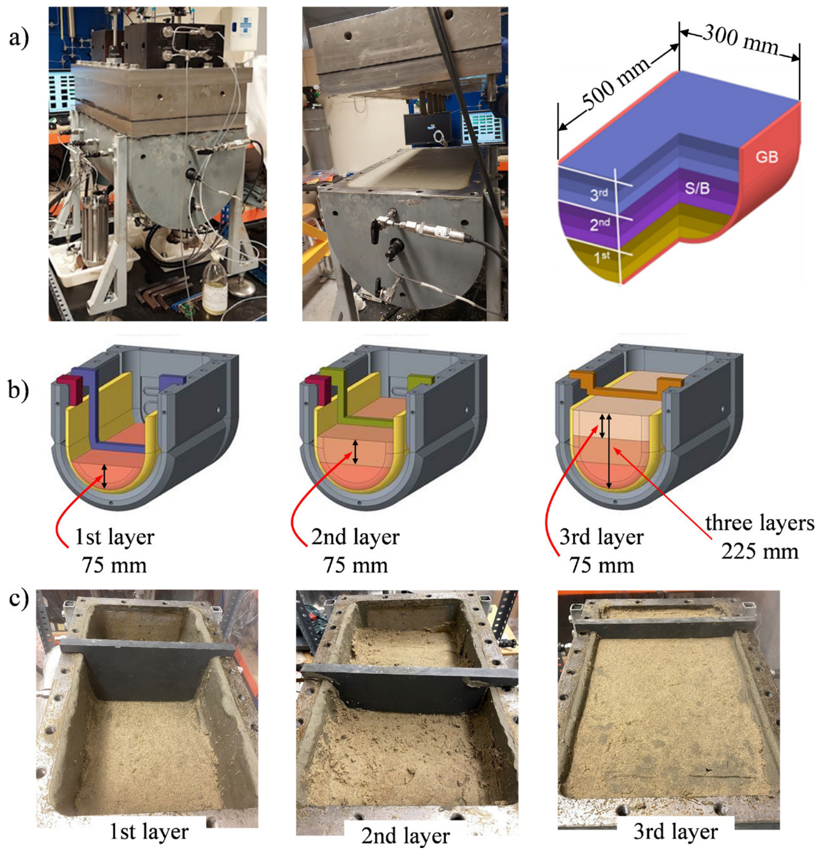

Figure 11. dm-scale mock-up developed at the Geotechnical Laboratory UPC to mimic field compaction of the GAST test and determine permeability parallel to dynamically compacted layers. (a) Photographs and schematics of the mock-up; (b) compaction layers; (c) 3D-printed tools to control compaction.

the S/B mixture were $w = (12.7\pm0.4)\%$ and $\rho_d = (1.66\pm0.01)$ Mg/m^3 (S_r around 0.56 with a maximum static fabrication stress of 1.0 MPa at s = 0.2 MPa). The density of the lifts was carefully controlled using 3D-printed tools (Figure 11c). The samples were prepared under high relative humidity to preserve their initial water content during the long-lasting, dynamic compaction process.

Figure 12 presents permeability results at the different scales, two orientations (horizontal flow parallel to compaction lifts and vertical flow) and varying *e*. The various scales of the laboratory tests corresponded to a) cm-scale oedometer tests (50 mm in diameter) for the vertical permeability after dynamic compaction; b) dm-scale infiltration tests in a cylindrical mould of 70 mm in diameter and 160 mm high in which the S/B was compacted in four layers (vertical flow orthogonal to compaction lifts); c) dm-scale mock-up tests described above with flow parallel to compaction layers; and d) m-scale tests for horizontal flow between piezometers installed in the GAST field test (injection flow rate and measured local pressures). The scale effects and anisotropic features are clearly shown in the figure. The induced anisotropy during laboratory compaction arises due to preferential vertical straining (transversally isotropic fabric), which affects the flow. The dm-scale infiltration column tests were performed with flow parallel to this vertical straining, which induced lower water permeability values (the flow is conditioned by the high-density zones at the top of the compacted layers with the lowest water permeability). As observed in the figure, consistent vertical permeability in terms of *e* was observed in the cm-scale element and dm-scale infiltration column tests (an expression is given in the figure for k_v as a function of *e*). On the other hand, layering, a larger-scale concept involving compaction interfaces, has been a significant issue in the mock-up and the field demonstration tests where the low-density zones condition the flow pathways (usually at the bottom of the compacted layers). A slightly larger horizontal permeability is detected at the field m-scale. The figure shows that the anisotropy ratio at approximately equivalent *e* is small and typically between $k_h / k_v = 3$ and 5.

6. Summary and concluding remarks

Different examples of compacted soils used in earthworks for hydraulic, environmental and energy applications were presented to motivate experimental research and techniques at various scales (mm-scale (micro), cm-scale (element

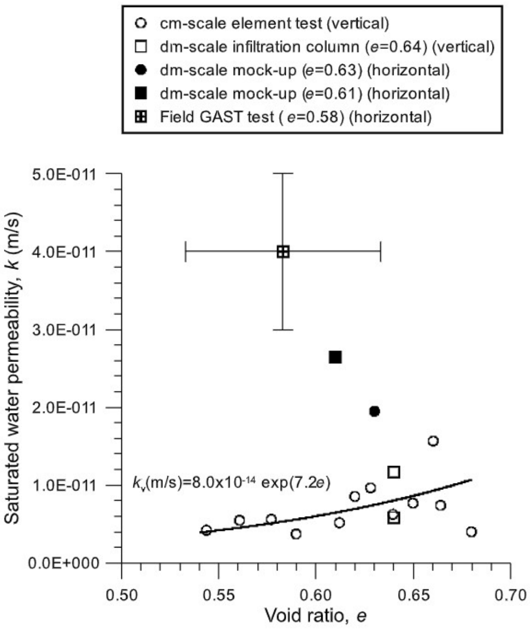

Figure 12. Saturated water permeability on S/B at different scales. cm-scale element tests, dm-scale infiltration column, and dm-scale mock-ups with flow parallel to compaction layers. GAST field test (water flow/piezometer data using injection flow rate and measured local pressures).

tests), dm-scale (mock-up tests), m-scale (demonstration/trial tests)). The paper showed the importance of selecting adequate techniques and improving experimental protocols to the appropriate length scale to capture different aspects of the behaviour of compacted soils (particular behavioural features were observed at specific length scales).

Although the experimental techniques cannot explain all the phenomena affecting compacted soils (mainly associated with the different preparation protocols followed in laboratory and field conditions), they highlight the critical role of the microstructure (aggregate size and inter-aggregate porosity) and the variability of soil properties at various scales. The contribution is helpful because it presents data on different compacted materials at multiple scales, ranging from mm- to m-scale, and they can help understand some fundamental issues observed at a larger scale.

Concerning the different experimental scales, we can indicate the following.

- Microstructural (mm-scale) and element tests (cm-scale). They help understand processes where the pore size and the aggregate/grain size distribution play an essential role (macropore connectivity between aggregates). Microstructural techniques are also helpful in validating and improving conceptual models of compacted soils. cm-scale element tests are convenient for first parameter estimation (permeability, water retention properties, volume changes on wetting, …) and for capturing processes under controlled initial state and boundary conditions (particle mobilisation during flow, temperature effects and chemically induced processes);
- High-quality mock-up tests (dm-scale). They help study the role of compaction layers, interfaces, and soil anisotropy under controlled initial state and boundary conditions. They are valuable in supporting larger-scale field tests. More realistic soil properties (permeability, compressibility) than element tests;
- Field/demonstration tests (m-scale). They are convenient for capturing larger-scale heterogeneous properties and assessing the impact of the compaction layers and interfaces on soil response (permeability and stiffness properties of compacted soils). Although the initial state and the boundary conditions are not so controlled. More realistic soil properties (permeability, compressibility) accounting for compaction layers, anisotropic features, and heterogeneity to predict the response of field applications;
- Model. Determine upscaled properties by considering heterogeneous zones and realistic boundary conditions (back-analysed parameters from field tests and monitoring data) to predict better the response of field applications with realistic boundary conditions and material properties (heterogeneous and anisotropic properties). Using the knowledge gained at different experimental scales is essential to help develop constitutive and numerical models to better upscale behavioural features of compacted soils.

Acknowledgements

Thanks are extended to Prof. Eduardo Alonso, Dr Núria Pinyol, Eng. Miguel Alonso, and Dr Clemente Mata associated with the design stage of the Albagés dam project. The help received from Dr Juliana Knobelsdorf during the preparation of the figures and data processing is acknowledged. The author acknowledges the financial support of the 'National Cooperative for the Disposal of Radioactive Waste' Nagra (Switzerland) through a competitive research project (GAST – Laboratory investigation of two-phase transport in sand-bentonite mixtures, ref 18311, 2019-2022) with the 'International Centre for Numerical Methods in Engineering' CIMNE (Spain), as well as Dr Clara Alvarado and Prof. Antonio Lloret for the associated experimental research. The author also thanks project PID2022-141429OB-I00 funded by the Spanish Ministry of Science/Research Agency MCIN/AEI/10.13039/501100011033/FEDER EU (2023-2027).

Declaration of interest

The author has no conflicts of interest to declare. There is no financial interest to report.

Data availability

The datasets generated and analysed in the course of the current study are available from the author upon request.

List of symbols and abbreviations

e	Void ratio: $e = e_M + e_m$
e_m	Microstructural void ratio (voids inside the aggregates to the volume of solids)
e_M	Macrostructural void ratio (voids between aggregates to the volume of solids)
k	Permeability
k_h	Horizontal permeability
k_v	Vertical permeability
s	Matric suction for tensiometer data and total suction for psychrometer data
RH	Relative humidity of the air
S_r	Degree of saturation
α, β	Parameters of Equation 1
ρ_d	Dry density
ρ_s	Density of solids

References

Alonso, E.E. (2014). Fracture mechanics and rockfill dams (Manuel Rocha lecture). *Soils and Rocks*, 37(1), 3-35. http://doi.org/10.28927/SR.371003.

Alonso, E.E., Gens, A., & Josa, A. (1990). A constitutive model for partially saturated soils. *Geotechnique*, 40(3), 405-430. http://doi.org/10.1680/geot.1990.40.3.405.

Alonso, E.E., Pinyol, N.M., & Gens, A. (2013). Compacted soil behaviour: initial state, structure and constitutive modelling. *Geotechnique*, 63(6), 463-478. http://doi.org/10.1680/geot.11.P.134.

Alonso, E.E., Romero, E., Arnedo, D., & Olivella, S. (2005). Geotechnical properties of low density unsaturated carbonated clayey silts and impact on the foundation of canal embankments. In *Proceedings of the 16th International Conference on Soil Mechanics and Geotechnical Engineering* (pp. 1823-1826), Osaka. Amsterdam: IOS Press. http://doi.org/10.3233/978-1-61499-656-9-1823.

Alonso, E.E., Tapias, M., & Gili, J. (2012). Scale effects in rockfill behaviour. *Géotechnique Letters*, 2(3), 155-160. http://doi.org/10.1680/geolett.12.00025.

Alonso, E.E., Vaunat, J., & Gens, A. (1999). Modelling the mechanical behaviour of expansive clays. *Engineering Geology*, 54(1-2), 173-183. http://doi.org/10.1016/S0013-7952(99)00079-4.

Casini, F., Vaunat, J., Romero, E., & Desideri, A. (2012). Consequences on water retention properties of double-porosity features in a compacted silt. *Acta Geotechnica*, 7(2), 139-150. http://doi.org/10.1007/s11440-012-0159-6.

Coop, M. (2024). The 7th Bishop Lecture: the mechanics of coarse-grained geomaterials at meso- and micro-scales. *Soils and Rocks*, 47(3), e2024006723. http://doi.org/10.28927/SR.2024.006723.

Cordão Neto, M.P., Lopes, B.C.F.L., Mascarenha, M.M.A., & Romero, E. (2017). A microstructural cam clay model for hydro-mechanical behavior of unsaturated soils. *Soils and Rocks*, 40(1), 3-16. http://doi.org/10.28927/SR.401003.

Della Vecchia, G., Jommi, C., & Romero, E. (2013). A fully coupled elatic-plastic hydromechanical model for compacted soils accounting for clay activity. *International Journal for Numerical and Analytical Methods in Geomechanics*, 37(5), 503-535. http://doi.org/10.1002/nag.1116.

Gonzalez-Blanco, L., Romero, E., Pinyol, N.M., & Alonso, E.E. (2023). Microstructure of compacted low-plasticity soils: the initial fabric and its evolution on stress and suction paths. *E3S Web of Conferences*, 382, 11003. http://doi.org/10.1051/e3sconf/202338211003.

Mora Ortiz, R.S. (2016). *Efectos de la microestructura en el comportamiento hidromecánico de suelos compactados* [Doctoral thesis, Universitat Politècnica de Catalunya]. Universitat Politècnica de Catalunya's repository (in Spanish). http://doi.org/10.5821/dissertation-2117-96315.

Nagra. (2024). *Gas-permeable seal test - setup and design.* Retrieved in July 15, 2024, from https://www.grimsel.com/gts-projects/gast/gast-setup-and-design

Pinyol, N.M., & Alonso, E.E. (2019). Design, construction, monitoring and modelling of Albagés earth dam: a case history. *International Journal of Civil Engineering*, 17(4), 501-513. http://doi.org/10.1007/s40999-018-0314-z.

Romero, E. (2013). A microstructural insight into compacted clayey soils and their hydraulic properties. *Engineering Geology*, 165, 3-19. http://doi.org/10.1016/j.enggeo.2013.05.024.

Romero, E., & Simms, P.H. (2008). Microstructure investigation in unsaturated soils: a review with special attention to contribution of mercury intrusion porosimetry and environmental scanning electron microscopy. *Geotechnical and Geological Engineering*, 26(6), 705-727. http://doi.org/10.1007/s10706-008-9204-5.

Romero, E., Della Vecchia, G., & Jommi, C. (2011). An insight into the water retention properties of compacted clayey soils. *Geotechnique*, 61(4), 313-328. http://doi.org/10.1680/geot.2011.61.4.313.

Romero, E., Alvarado, C., & Lloret, A. (2023). New challenges in experimental unsaturated soil mechanics: experimental upscaling of an engineered gas-permeable seal. *E3S Web of Conferences*, 382, 05001. http://doi.org/10.1051/e3sconf/202338205001.

Rüedi J., Teodori S.-P., Spillmann T., Reinhold M., Trick T., Keller M., Steiner P., Isler S., Gräfe K., García-Siñeriz Martínez J.-L., Palacios J.B., Jacobs F., Eiholzer L., Maurer H., Tisato N., & Marelli S. (2012). *Gas-permeable seal* *test at GTS: as built report* (Nagra Tech. Report, No. NAB 12-59). Wettingen: Nagra Arbeitsbericht.

Sakaki, T., Sakabayashi, K., Kawamoto, K., & Spillmann, T. (2023). Compaction-induced variability in the 80/20 sand-bentonite mixture: spatial variation in dry density at different scales in the laboratory and large-scale gas seal test. *Applied Clay Science*, 246, 107146. http://doi.org/10.1016/j.clay.2023.107146.

Yin, P., & Vanapalli, S.K. (2022). Model for predicting evolution of microstructural void ratio in compacted clayey soils. *Canadian Geotechnical Journal*, 59(9), 1602-1621. http://doi.org/10.1139/cgj-2021-0057.

Yuan, S., Liu, X., Romero, E., Delage, P., & Buzzi, O. (2020). Discussion on the separation of macropores and micropores in a compacted expansive clay. *Géotechnique Letters*, 10(3), 454-460. http://doi.org/10.1680/jgele.20.00056.